Challenges in isolating primary remanent magnetization from Tethyan carbonate rocks on the Tibetan Plateau: Insight from remagnetized Upper Triassic limestones in the eastern Qiangtang block

Wentao Huang [a,*], Michael J. Jackson [b], Mark J. Dekkers [c], Yang Zhang [d], Bo Zhang [d], Zhaojie Guo [d], Guillaume Dupont-Nivet [d,e,f]

[a] *Department of Earth and Environmental Sciences, University of Rochester, Rochester, NY 14627, USA*
[b] *Institute for Rock Magnetism, Department of Earth Sciences, University of Minnesota, MN, USA*
[c] *Department of Earth Sciences, Utrecht University, Utrecht, the Netherlands*
[d] *Key Laboratory of Orogenic Belts and Crustal Evolution, Ministry of Education, School of Earth and Space Sciences, Peking University, Beijing, China*
[e] *University of Rennes 1, CNRS INSU UMR 6118, Geosciences, Rennes, France*
[f] *Institute for Earth and Environmental Science, Universität Potsdam, Potsdam, Germany*

ARTICLE INFO

ABSTRACT

Carbonate rocks, widely used for paleomagnetically quantifying the drift history of the Gondwana-derived continental blocks of the Tibetan Plateau and evolution of the Paleo/Meso/Neo-Tethys Oceans, are prone to pervasive remagnetization. Identifying remagnetization is difficult because it is commonly undetectable through the classic paleomagnetic field tests. Here we apply comprehensive paleomagnetic, rock magnetic, and petrographic studies to upper Triassic limestones in the eastern Qiangtang block. Our results reveal that detrital/biogenic magnetite, which may carry the primary natural remanent magnetization (NRM), is rarely preserved in these rocks. In contrast, authigenic magnetite and hematite pseudomorphs after pyrite, and monoclinic pyrrhotite record three episodes of remagnetization. The earliest remagnetization was induced by oxidation of early diagenetic pyrite to magnetite, probably related to the collision between the northeastern Tibetan Plateau and the Qiangtang block after closure of the Paleo-Tethys Ocean in the Late Triassic. The second remagnetization, residing in hematite and minor goethite, which is the further subsurface oxidation product of pyrite/magnetite, is possibly related to the development of the localized Cenozoic basins soon after India-Asia collision in the Paleocene. The youngest remagnetization is a combination of thermoviscous and chemical remanent magnetization carried by authigenic magnetite and pyrrhotite, respectively. Our analyses suggest that a high supply of organic carbon during carbonate deposition, prevailing sulfate reducing conditions during early diagenesis, and widespread orogenic fluid migration related to crustal shortening during later diagenesis, have altered the primary remanence of the shallow-water Tethyan carbonate rocks of the Tibetan Plateau. We emphasize that all paleomagnetic results from these rocks must be carefully examined for remagnetization before being used for paleogeographic reconstructions. Future paleomagnetic investigations of the carbonate rocks in orogenic belts should be accompanied by thorough rock magnetic and petrographic studies to determine the origin of the NRM.

1. Introduction

The Tibetan Plateau is made of a series of continental blocks that rifted away from Gondwana in the south and subsequently drifted towards and collided with Eurasia in the north from Meso-zoic to Cenozoic times (Yin and Harrison, 2000). The process was accompanied by opening and closing of the Pale-, Meso-, and Neo-Tethys oceans, resulting in the formation and subsequent deformation of abundant marine carbonate rocks preserved today in the Himalayas and Tibetan Plateau. From north to south (Figs. 1a, b), these continental blocks include the Qiangtang, which welded to the south of northeastern Tibet along the Jinsha suture after closure of the Paleo-Tethys Ocean in the Late Triassic (e.g., Yin and Harrison, 2000; Song et al., 2015); the Lhasa block, which collided
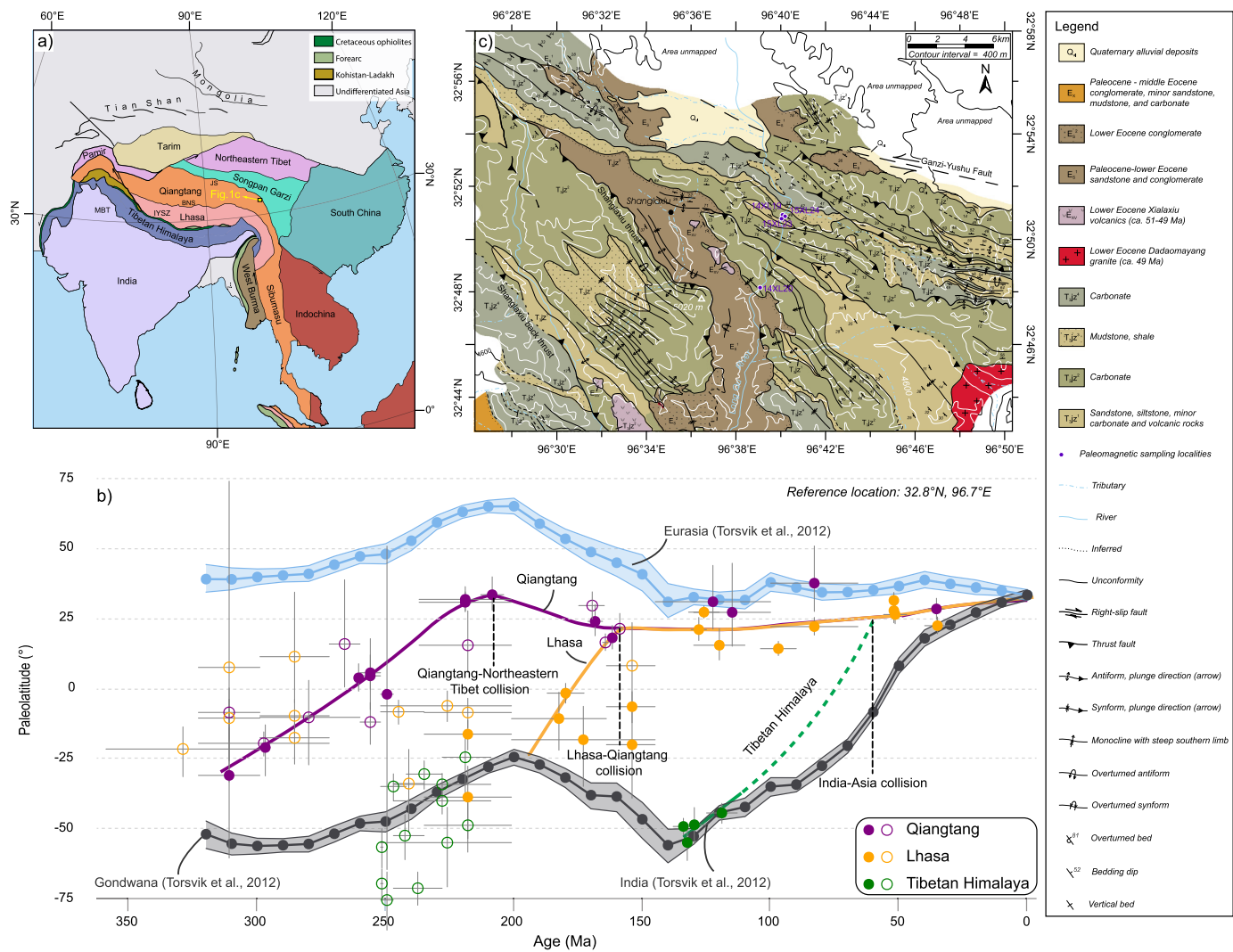
Fig. 1. (a) Tectonic map of the India-Asia collision zone (modified from van Hinsbergen et al., 2012). (b) Paleolatitude versus time plot with paleomagnetic data from the Tibetan Himalaya, Lhasa, and Qiangtang blocks in the Tibetan Plateau generated using www.paleomagnetism.org (Koymans et al., 2016). Circles represent paleomagnetic poles determined by carbonate rocks. Dots are from clastic and volcanic rocks. Paleomagnetic data are from Song et al. (2017), updated with the latest reported poles (Bian et al., 2017; Ma et al., 2018, 2019; Cao et al., 2019). (c) Geologic map of the Yushu-Nangqian area with paleomagnetic sampling localities of the Upper Triassic limestones plotted. (For interpretation of the colors in the figure(s), the reader is referred to the web version of this article.)

with the Qiangtang block along the Bangong-Nujiang suture zone after closure of the Meso-Tethys Ocean in the Late Jurassic to Early Cretaceous (e.g., Kapp et al., 2007); and the Tibetan Himalaya, the northernmost continental unit of the Indian plate, which collided with the Lhasa block along the Indus-Yarlung suture zone after closure of the Neo-Tethys Ocean in the early Paleogene (e.g., Hu et al., 2015). Large-scale south-north motion of these blocks took place during their transfer from Gondwana to Eurasia, which makes paleomagnetism one of the most important tools to decipher the opening and closing of the Tethys Oceans, the drifting and collision of these continental blocks, and the kinematic evolution and tectonic history of the Himalayas and Tibetan Plateau.

The widely distributed carbonate rocks on the Himalayas, the Lhasa and Qiangtang blocks, have been one of the main targets for paleomagnetic studies to constrain the paleolatitude drift history of these blocks (circles in Fig. 1b). Paleomagnetic studies on these rocks started in the 1980s and 1990s (see summary in van Hinsbergen et al., 2012), and these pioneering studies have been greatly improved recently by acquiring larger datasets and applying more sophisticated analytical techniques for the Himalayas (e.g., Huang et al., 2015), the Lhasa block (e.g., Bian et al., 2017; Ma et al., 2018), and the Qiangtang block (e.g., Cao et al., 2019).

Nevertheless, results reported from these carbonate rocks are disparate, and often contradict the usually more robust paleomagnetic results determined from coeval volcanic and fine-grained detrital rocks. For example, estimated Triassic paleolatitudes of the Tibetan Himalaya based on data from carbonate rocks range from 75.7°S to 24.8°S (reference location: 32.8°N, 96.7°E, same for below) (Fig. 1b), and most deviate from the predicted paleolatitudes from the global apparent polar wander path (GAPWaP, Torsvik et al., 2012). Paleomagnetic results from carbonate rocks have been interpreted to indicate that the Lhasa block was located at low southern hemisphere latitudes during Carboniferous-Triassic times, whereas the GAPWaP of Gondwana predicts middle-high southern hemisphere latitude (Fig. 1b). The Late Triassic latitude of the Qiangtang block was constrained to be ~15°N from data from limestones (Zhou et al., 2017), much lower than the robust results of 30–33°N from volcanic rocks (Fig. 1b) (Song et al., 2015).

Although potential inclination shallowing induced by compaction might contribute to the abnormality in these datasets (Kodama, 2012), widespread remagnetization of carbonate rocks, as recognized in the orogenic belts in North America, South America, and Europe (Elmore et al., 2012; van der Voo and Torsvik, 2012, and references therein), must also be considered. Remagne-

tization of carbonate rocks has been documented in the Himalayas of the India-Asia convergence zone, which significantly affects constraints on the dimension of Greater India and thus our understanding of the intricacies of the India-Asia collision. In the Himalayan metacarbonate rocks, pervasive remagnetizations residing in pyrrhotite, formed by desulphidation of pyrite or breakdown of magnetite under reducing conditions, have been identified and postdate the main Cenozoic Himalayan folding (Appel et al., 2012, and references therein). In the Jurassic-Lower Paleogene Himalayan limestones that have not been metamorphosed, we have found that oxidation of early diagenetic pyrite to authigenic magnetite has induced pervasive remagnetization of these rocks (Huang et al., 2015, 2017a,b). This leads us to propose rock magnetic and petrographic criteria for identifying remagnetization in limestones, and these criteria are invaluable when routine field tests cannot be trusted (Huang et al., 2017b). Indeed, although most paleomagnetic studies on these Carboniferous-Jurassic limestones from the Tethyan Himalaya, Lhasa, and Qiangtang blocks have provided positive fold or reversals tests to support a primary origin of their isolated characteristic remanent magnetization, these test do not preclude remagnetization during lithification of flat lying sediments much later than the deposition attending closure of Paleo/Meso/Neo-Tethys Oceans and subsequent continental collisions. Remagnetization processes may have expanded dual geomagnetic polarities, yielding apparent positive reversals tests. The uncertainties in the classic field tests call for determining the origin of the NRM by investigating the characteristics of its carrier(s), which can actually be accomplished by thorough rock magnetic analyses and petrographic observations.

To test whether primary NRMs are preserved, and to identify the mechanisms for potential remagnetization, we present paleomagnetic, rock magnetic, and petrographic results from Upper Triassic limestones in the eastern Qiangtang block of the Tibetan Plateau. We isolated remanent magnetizations, applied high-temperature, room-temperature, and low-temperature rock magnetic experiments, and examined thin sections by scanning electron microscopy (SEM) and energy-dispersive X-ray spectrometry (EDS). Collectively, we evaluated the origin of the remanent magnetizations, interpreted their acquisition mechanisms, and discussed the implications for preservation of primary remanent magnetization in the Tethyan carbonate rocks in the Tibetan Plateau.

2. Geologic background and paleomagnetic sampling

The Qiangtang block, one of the major Gondwana-originated units of the Tibetan Plateau, is bounded by the Jinsha suture to the north and Bangong-Nujiang suture to the south (Fig. 1a). It is east-west-trending with a maximum width of 400–500 km in the western and middle parts, but changes into a north-south orientation and narrows to <150 km in the eastern part (Fig. 1a). The study area is located in the north of the Yushu-Nangqian area in the eastern Qiangtang block, where the major stratigraphic units are Upper Triassic shallow-water marine carbonates and minor clastic rocks, deposited on the northern passive margin of the Qiangtang block, and overlying Paleogene red beds (Fig. 1c, Spurlin et al., 2005). The Upper Triassic strata are the Jieza Group (T_3jz), which contains four units of T_3jz^1, T_3jz^2, T_3jz^3, and T_3jz^4 from bottom to top. The T_3jz^1 consists of sandstone, siltstone, and minor carbonate and volcanic rocks; The T_3jz^3 is dominated by mudstone and shale; The T_3jz^2 and T_3jz^4 are composed of carbonate rocks. Cenozoic strata unconformably overlie the Jieza Group, and contain conglomerate, sandstone, and minor mudstone and carbonate. Pre-Cenozoic deformation of the Upper Triassic strata is indicated by the angular unconformity between tightly folded Upper Triassic and mostly flat-lying Cenozoic strata (Fig. 1c), as along the Ganzi-Yushu fault at the northern margin of the Shanlaxiu basin,

where carbonate deformation was proposed to relate to Late Triassic closure of the Paleo-Tethys ocean (Spurlin et al., 2005). Cenozoic folding and thrusting of the Upper Triassic strata are also common, as best observed along the Shanglaxiu thrust farther south, and can be clearly distinguished from an earlier deformation phase (Fig. 1c).

We have focused on limestones from the well-exposed T_3jz^2 along road cut exposures. Standard paleomagnetic cores with a diameter of 2.5 cm were collected at four sites (14XL19, 14XL20, 15XL23, and 15XL24) using a portable gasoline-powered drill (Fig. 1c). Samples were oriented with magnetic and sun compasses. In each site, the distance between adjacent cores is 0.5–1 m in stratigraphic level. Specially, there are fourteen, eighteen, and sixteen cores collected from 14XL19, 15XL23, and 15XL24, respectively. These three sites are non-reddish and far away from the Cenozoic strata. The other site (14XL20) is reddish and lies just below the unconformity between the T_3jz^2 and Cenozoic Shanglaxiu basin strata and eighteen cores were collected.

3. Paleomagnetism

We isolated remanent magnetizations from these limestones by progressive thermal demagnetization. Successive temperature steps at 130, 170, 210, 250, 290, 330, 370, 410, 450, 480, 510, 540, 570, and 600 °C were applied for samples from 14XL19, 15 XL23, and 15XL24, and steps at 130, 170, 210, 250, 290, 330, 370, 410, 450, 490, 530, 570, 610, 640, and 670 °C were applied for the reddish samples from 14XL20, until complete demagnetization of the NRM. Remanence was measured using a 2G Enterprises DC SQUID magnetometer (noise level $1-2 \times 10^{-12}$ A m^2) installed in the magnetically shielded room at University of Rennes1 (France). Principal component analysis was used to precisely determine the direction of remanent magnetizations (Kirschvink, 1980). The defined directions are presented in Table S1.

For samples from the non-reddish sites (14XL19, 15XL23, and 15XL24), thermal demagnetization reveals a low-temperature component (LTC) and an intermediate-temperature component (ITC) with laboratory unblocking temperatures between 130 °C and ~250–330 °C, and between ~290–330 °C and 570 °C, respectively (Figs. 2a–d, i–p). Most samples from 14XL20 have one component with wide unblocking temperature range from 130 °C to 670 °C (Figs. 2e, h). Interestingly, one sample from this site reveals a LTC isolated between 130 °C and 250 °C, and an ITC isolated between 250 °C and 530 °C (Fig. 2f). Another sample yields three components with a LTC (130–290 °C), an ITC (290–530 °C) and a high-temperature component (HTC, 530–630 °C) (Fig. 2g). The LTCs from these two samples are of normal polarity, whereas the ITCs have reverse polarity (Figs. 2f, g).

Directions of the LTCs from the reddish sites (14XL20) are similar to those of the LTCs from the other sites (14XL19, 15XL23, and 15XL24). Together, they define a mean direction of $D_g = 7.3°$, $I_g = 49.7°$ ($n = 38$, $k = 76.2$, $a_{95} = 2.7°$, "g" stands for geographic coordinates), which is indistinguishable from the direction of the present day magnetic field (PDF) at the sampling localities (Fig. 3a). The ITCs from 14XL19, 15XL23, and 15XL24 yield a mean direction of $D_g = 103.3°$, $I_g = 89.1°$ ($n = 36$, $k = 106.8$, $a_{95} = 2.3°$) before tilt correction, and $D_s = 36.4°$, $I_s = 46.9°$ ($n = 36$, $k = 135.2$, $a_{95} = 2.1°$, "s" stands for stratigraphic coordinates) after 100% tilt correction (Figs. 3a, b). The mean direction of the two ITCs of reverse polarity from 14XL20 is nearly antipodal to the mean direction of the other components isolated from samples in this site before tilt correction (Fig. 3a). After tilt correction, the mean direction of the isolated components is $D_s = 8.2°$, $I_s = 63.6°$ ($n = 15$, $k = 101$, $a_{95} = 3.8°$) (Fig. 3b). Robust field tests are not available for these carbonate rocks because the bedding orientation is uniform and the isolated remanence components are mostly of nor-
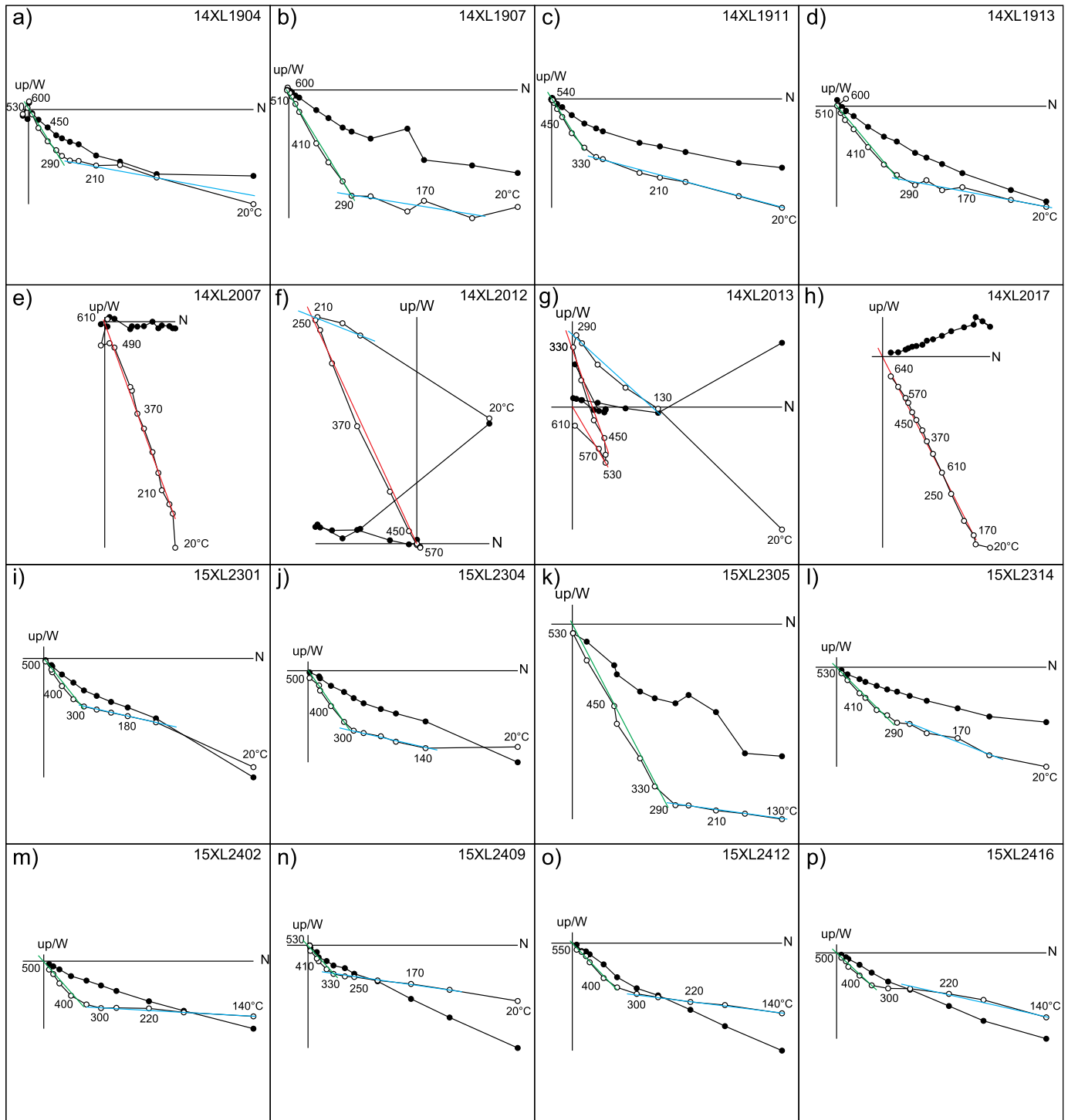
Fig. 2. Demagnetization diagrams for representative specimens. All diagrams are displayed after bedding tilt correction. Closed (open) symbols represent the projection of vector endpoints on the horizontal (vertical) plane; values represent the thermal demagnetization step. Lines are fitted directions for the isolated remanence. Blue lines are low-temperature components. Green lines are intermediate-temperature from sites 14XL19, 15XL23, and 15XL24; red lines are intermediate-temperature and high-temperature components from site 14XL20.

mal polarity. Therefore, we applied the following rock magnetic and petrographic tests to identify potential remagnetization and investigate the origin of the remanence.

4. Rock magnetism

To characterize the magnetic mineralogy and grain size of the limestones, a series of rock magnetic experiments were conducted

at the Utah Paleomagnetic Center at the University of Utah (USA), and the Institute for Rock Magnetism at the University of Minnesota (USA). A MicroMag Princeton Measurements vibrating sample magnetometer (VSM, nominal sensitivity of 5×10^{-9} A m^2) was used for magnetic hysteresis measurements on 21 samples (nine from 14XL19, three from 14XL20, six from 15XL23, and three from 15XL24) at room temperature and 1 sample (14XL1904) at 29 low temperature steps (20–300 K with temperature increment
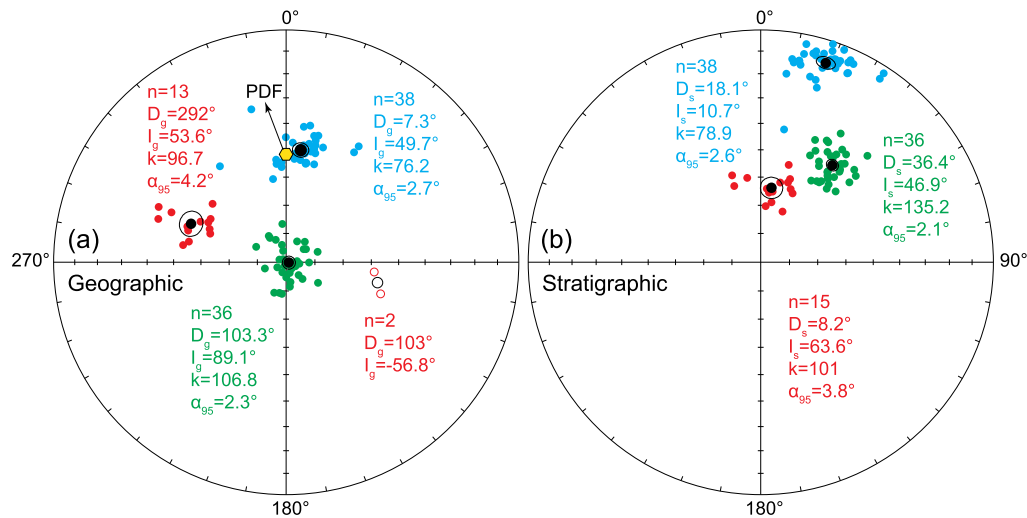
Fig. 3. Equal-area projections of the isolated remanent magnetization directions by line fits in geographic (a) and stratigraphic coordinates (b). Blue dots are low-temperature components from all sites; green dots are intermediate-temperature component from sites 14XL19, 15XL23, and 15XL24; red dots (circles) are isolated remanence from site 14XL20. Small black dots (circles) represent the mean remanence directions, big circles are the corresponding 95% confidence limit. The two remanence directions from site 14XL20 with reversal polarity in geographic coordinates were transferred to normal polarity for the calculation of the mean direction in stratigraphic coordinates.

of 10 K). High-temperature magnetic susceptibility measurements were performed in air on seven whole-rock samples using a KLY-2 KappaBridge AC susceptibility meter with an AC field of 300 A/m and a frequency of 920 Hz. Five cycles of successive heating to 300 °C, 400 °C, 500 °C, 600 °C, and 700 °C with intervening cooling to room temperature were carried out on one sample. Two samples were subjected to the first four cycles up to 600 °C, and the remaining three samples underwent successive cycles to 300 °C, 500 °C, 600 °C, and 700 °C. Low-temperature remanence and alternating current (AC) susceptibility experiments were run on a Quantum Design Magnetic Properties Measurement System (MPMS-5S). Methods used for the analyses on the MPMS are the same as those described in Huang et al. (2017b). Four samples (one from each of the four sites) were subjected to low-temperature magnetic characterization, beginning with room-temperature saturation isothermal remanent magnetization (RTSIRM given in 2.5 T) measured in zero field during cooling to 20 K and on rewarming back to RT. Next, samples were field cooled (FC) to 20 K in 2.5 T field, the field was removed upon reaching 20 K, and they were measured in zero field on rewarming to RT. Finally, they were zero-field cooled (ZFC) to 20 K, given a low-temperature saturation isothermal remanent magnetization (LTSIRM) in 2.5 T at 20 K, and measured in zero field during warming to RT. Four more samples (two from each of 14XL19 and 15XL23) were characterized using an abbreviated subset of experiments (RTSIRM cooling and ZFC warming measurements), and three samples (one from each of sites 14XL19, 15XL23, and 15XL24) were run for low-temperature susceptibility measurements at five frequencies (1.0, 5.6, 31.6, 177.9, and 997.3 Hz).
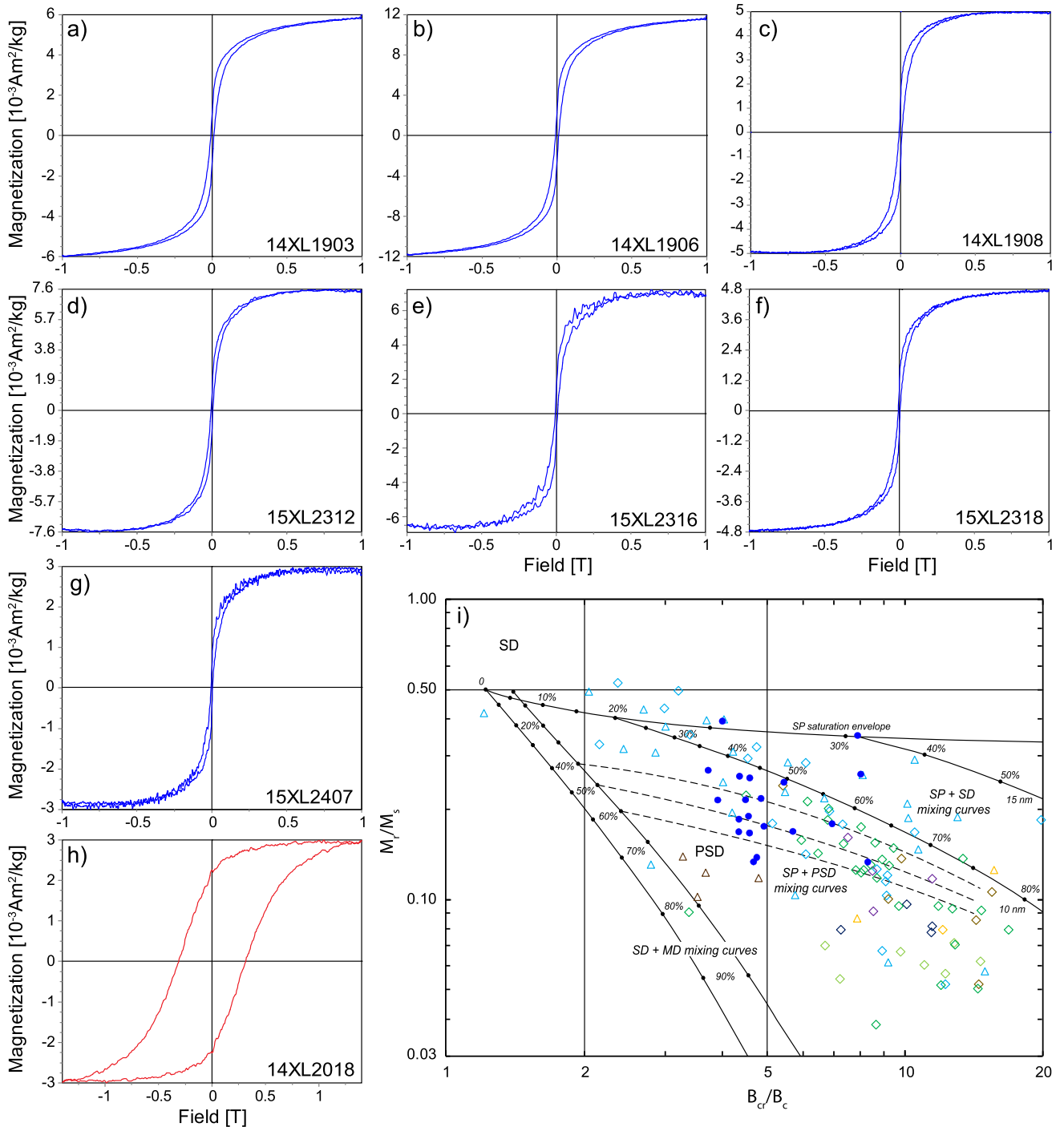
4.1. Room-temperature hysteresis measurements

Hysteresis curves for the specimens from the non-reddish sites 14XL19, 15XL23, and 15XL24 are 'wasp-waisted' (Figs. 4a–f), indicating the existence of multiple magnetic components with distinct coercivities, which may correspond to mixtures of magnetic minerals, or different size fractions of a single mineral (Tauxe et al., 1996). The low coercive force (B_c) and remanent coercivity (B_{cr}) values for these specimens indicate that the dominant magnetic carrier has a low coercivity (Table S2). Some of these specimens are saturated at 0.5 T, others show a slow increase of magnetization up to 1 T. These observations suggest that the dominant

magnetic carriers in these limestones are probably magnetite with contrasting grain sizes. A small fraction of hematite is also indicated in some specimens. On the Day plot (Fig. 4i), hysteresis parameters of specimens from these sites plot in the region with mixtures of superparamagnetic (SP) and single domain (SD) or pseudosingle domain (PSD) magnetite (Dunlop, 2002). Their Day plot positions thus overlap with the range of data from remagnetized Tethyan Himalayan limestones and remagnetized carbonates elsewhere, and differ from that of the carbonates with primary remanent magnetization (e.g., Jackson and Swanson-Hysell, 2012; Roberts et al., 2013; Huang et al., 2017b). In contrast, specimens from the reddish site 14XL20 are characterized by rectangular hysteresis loops and very high remanent coercivity values (Figs. 4g, h; Table S2), consistent with the dominance of hematite in these specimens.

4.2. High-temperature susceptibility

High-temperature magnetic susceptibility versus temperature curves of most specimens are characterized by two quasi-linear and reversible descending trends of the susceptibility with an inflection point at ∼500 °C (Figs. 5b–d). Below 500 °C, these specimens lost >50% of their susceptibility. Above 500 °C, the susceptibility decrease shows a steeper slope, with no sharp drop in magnetic susceptibility. This is clearly shown in most specimens, except for 15XL2318, which shows a prominent decrease in magnetic susceptibility near the Curie temperature of magnetite. These observations are consistent with the presence of fine-grained magnetite and minor hematite in specimens from the non-reddish sites 14XL19, 15XL23, and 15XL24, and the dominance of fine-grained hematite in specimens from the reddish site 14XL20 (Dunlop and Ödemir, 1997). Remarkably, three specimens show strikingly different behavior above 400 °C (Figs. 5a, e, f). For 15XL2405, a large increase in magnetic susceptibility is observed at 425–570 °C on heating curves, followed by a sharp decrease at higher temperatures. The cooling curve is irreversible. This behavior is attributed to magnetite production due to the breakdown of pyrite (Zegers et al., 2003). For 14XL1908 and 15XL2318, a distinct drop in magnetic susceptibility on heating with irreversible cooling paths takes place between 400 and 500 °C, suggesting finer grain size magnetite.

Fig. 4. (a–h) Room-temperature magnetic hysteresis loops from representative specimens after correction for the paramagnetic/diamagnetic/antiferromagnetic contribution. All the loops for specimens from sites 14XL19, 15XL23, and 15XL24 are 'wasp-waisted'. (i) Day plot of the hysteresis parameters for specimens from sites 14XL19, 15XL23, and 15XL24 in this study (blue dots), and the remagnetized Jurassic-Paleogene Tethyan Himalayan limestones (triangles and diamonds) presented in Huang et al. (2017b).

4.3. Low-temperature magnetic properties

4.3.1. Low-temperature hysteresis measurements

Hysteresis loops of 14XL1904 show strong and progressive rise in remanent saturation (M_s), saturation magnetization (M_{rs}), B_c, and B_{cr} values as the SP fraction of magnetite blocks when the measurement temperature reduces stepwise from room temperature to 20 K (Fig. 6; Table S3). The constriction of the hysteresis loops gradually weakens weaker and loops transform to pot-bellied shapes at low temperature. Upward shift and broadening of the M_{rh} curves with decreasing temperature shows that the hystere-

sis loops widen (Fig. 6c). Quantitative loop analysis indicates that M_s, M_{rs}, B_c, and B_{cr} values increase to ∼2 times their room-temperature values at 40 K (Figs. 6d, e). The sharp increase in M_s value below 40 K is possibly induced by non-linear paramagnetic signal that affects the approach-to-saturation calculations, or ordering of some iron-bearing phases. The shape parameter σ shows that the dramatic change from 'wasp-waisted' loop shapes to pot-bellied shapes occurs below 30 K (Fig. 6f). These observations are consistent with a gradual transition of the SP-stable single domain (SSD) threshold toward smaller magnetite grain sizes on cooling.
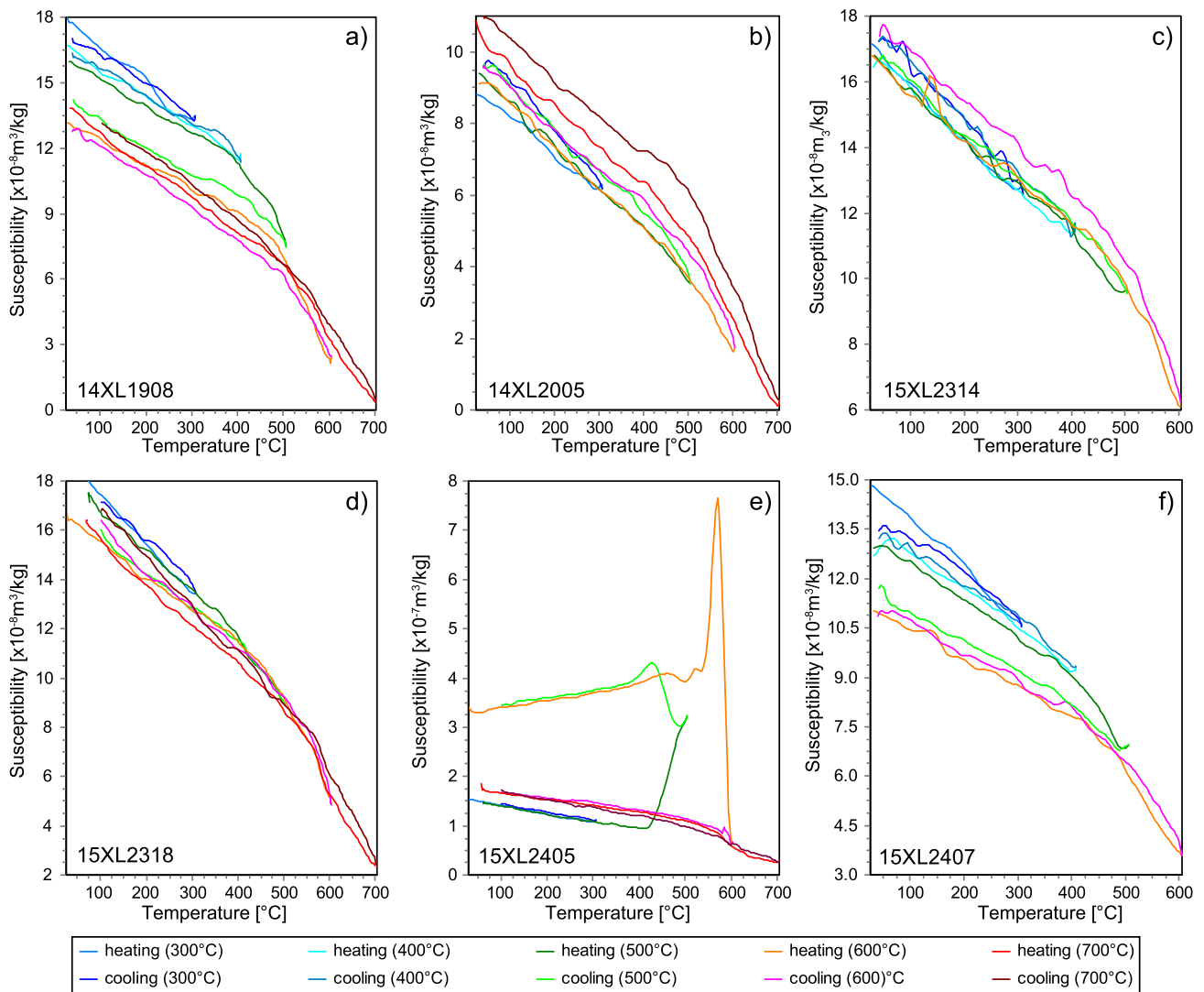
Fig. 5. Multicycle high-temperature bulk magnetic susceptibility measurements in air for representative specimens.

4.3.2. Low-temperature cycling of RTSIRM and SIRM warming

The low-temperature cooling curves of a RTSIRM for most specimens from the non-reddish sites 14XL19, 15XL23, and 15XL24 show increases in remanence on cooling, followed by a small drop in magnetization at ∼225 K, which is also clearly shown in the derivative curves (Figs. 7a–d, i–l, 8a, i), and is thus probably related to the Morin transition in fine-grained hematite. The fact that the drop is lower than the classic Morin transition at 250–260 K likely relates to the finer hematite grain size in these limestones (Özdemir et al., 2008). After this small drop, the remanence of these specimens remains stable or decreases slightly to 175 K, and then descends quickly. However, derivatives of the RTSIRM cooling curves do not show the characteristic magnetite Verwey transition (T_v) except for specimens from 15XL2304, although magnetite is the dominant magnetic carrier. When the temperature falls below 40 K, a sharp decrease of the remanence appears in some samples (Figs. 7a–b, 8a) and is clearly expressed in the derivative curves (Figs. 7i–k, 8i–k). It is possibly associated with the Besnus transition in monoclinic pyrrhotite at ∼34 K (Dekkers et al., 1989). A prominent feature in the warming curves of the RTSIRM is a "hump" in remanence between 150 K and 200 K, which is the hallmark feature of oxidized magnetite (Özdemir and Dunlop, 2010). Specimens 15XL2312 and 15XL2317 (Figs. 8b–c) show a monotonic increase in remanence until 40 K in the cooling curves and

reversible warming curves, suggesting strong maghemitization of magnetite, and existence of goethite (Dunlop and Ödemir, 1997). Derivatives of the RTSIRM cooling curves of 15XL2312 have a peak at 110-120 K, indicating a small contribution of magnetite. The low-temperature cycling curves of a RTSIRM for specimen from the reddish site 14XL20 undergo a progressive decrease in remanence on cooling, with a small amount (∼6%) of loss in remanence when warming back to room temperature and no Morin transition displayed (Figs. 8d, l), suggesting that the dominant hematite grain is nanosized (De Boer et al., 2001).

The low-temperature SIRM warming curves after ZFC and FC treatment for specimens from the non-reddish sites 14XL19, 15XL23, and 15XL24 show a continuous decay in remanence during warming to room temperature with more than half of the low-temperature remanence at 20 K erased by warming to room temperature (Figs. 7e–h, 8e–g), implying that more than half of the ferromagnetic material is superparamagnetic at room temperature and does not contribute to the NRM. FC remanence is stronger than that of the ZFC, but the difference is very small for most specimens from sites 14XL19, 15XL23, and 15XL24 (Figs. 7g–h). No clear Morin transition is recognized, but some specimens show a very weak Verwey transition as distinguished in the derivatives of the FC curves (Figs. 7j, k, 8i–k). Large separation between FC and ZFC curves can be seen in 15XL2312, and possibly also in sample
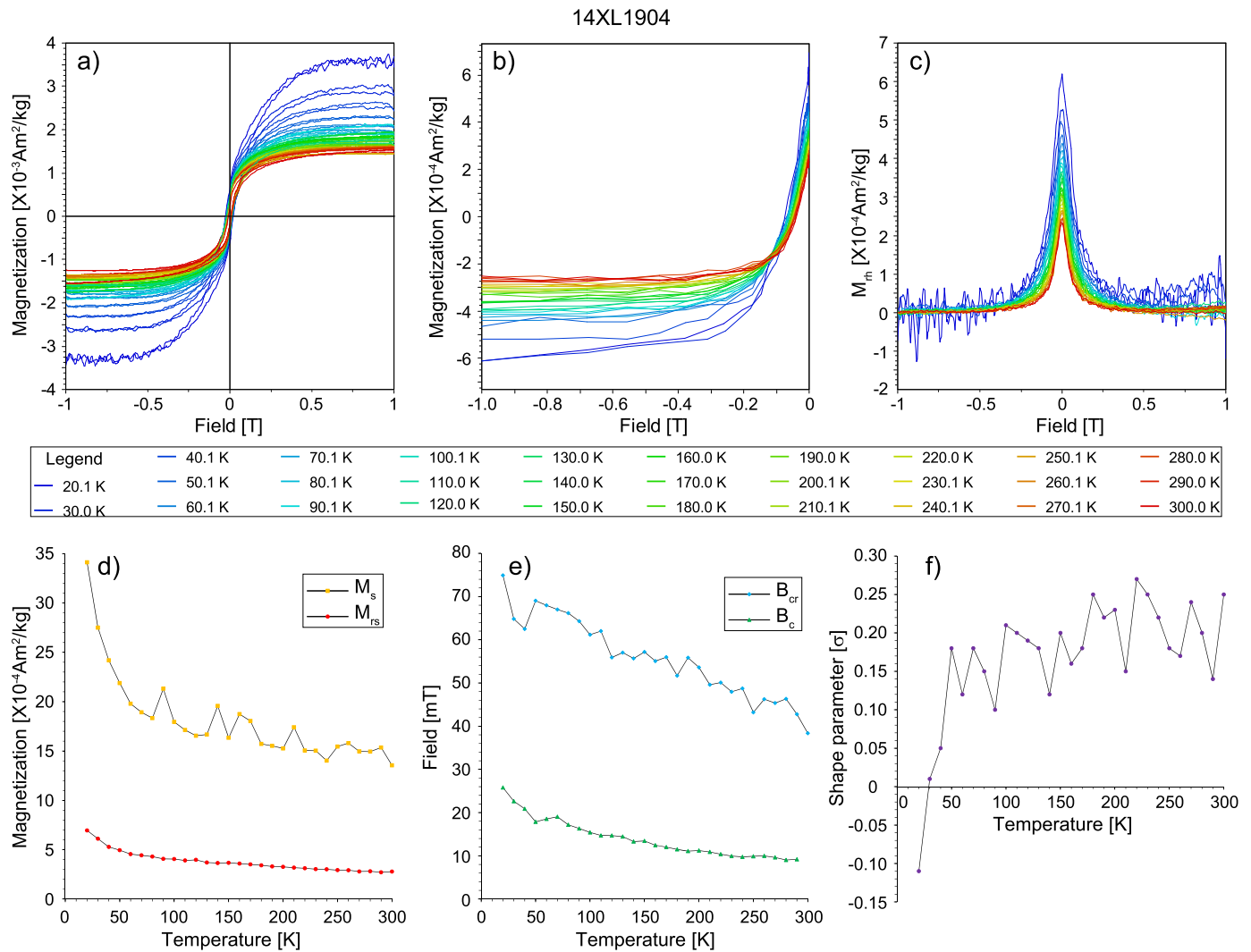
14XL1904

Fig. 6. (a–c) Low-temperature magnetic hysteresis loops (a), back field curves (b), and M_{rh} curves (c) for specimen 14XL1904 measured at 29 steps. Hysteresis loops have been corrected for paramagnetic contribution. (d–f) Saturation magnetization (M_s), saturation remanent magnetization (M_{rs}), coercive force (B_c), remanent coercive (B_{cr}), and shape parameter (σ) as a function of decreasing temperature for 14XL1904.

15XL2317, which is typically attributed to the strong contribution of goethite. 14XL2018 from the reddish site shows characteristic concave FC and ZFC curves, these curves are also separated (Fig. 8h), indicating small contribution of goethite besides dominant fine-grained hematite. For ZFC curves showing no Verwey transition, magnetite grain size distribution can be calculated using the method of Worm and Jackson (1999). The inferred broad, unimodal size distribution of the SP magnetite (Figs. 7m, n), peaking at $\sim 10^{-24}$ m^3 (10 nm in diameter), is in good agreement with the modeled SP-SD or SP-PSD mixing curves in Fig. 4i (Dunlop, 2002).

4.3.3. Low-temperature AC susceptibility

The ferrimagnetic in-phase susceptibility (χ') at multiple frequencies for all specimens from the non-reddish sites 14XL19, 15XL23, and 15XL24 is presented after subtraction of the paramagnetic contributions based on Curie-Weiss paramagnetic temperature dependence (Fig. 9). At room temperature, a relatively strong frequency dependence of susceptibility is clearly shown with χ' at 1.0 Hz >20% higher than that at 997.3 Hz, indicating a significant fraction of grains with diameters below 15–25 nm (Worm, 1998). χ' for all specimens shows sharper increase on warming below 40 K (especially for 14XL1904), which may be attributed to the presence of minor pyrrhotite, as also shown by RTSIRM

cooling curves (Figs. 7, 8). After that, a nearly linear increase in χ' at higher temperatures is observed. Together with the strong frequency dependence of χ' over the entire temperature range, a wide distribution of grain sizes/unblocking temperatures for magnetite is implied. Out-of-phase susceptibility (χ'') is roughly 10 times lower than χ', and is noisier with increasing measurement frequency (Fig. 9). A sharp peak in χ'' observed below 40 K for all frequencies may also be induced by pyrrhotite. At higher temperatures, χ'' mimics the linear increase of χ' with the magnitude doubled from 50 K to 300 K. In general, χ'' at each temperature is in excellent quantitative agreement with the calculated values of $-(\pi/2)\, d\chi'/d(\ln(f))$ from Néel's single-domain theory (f is the measurement frequency), implying that χ'' originates from short-period viscosity of SP particles.

In summary, rock magnetic analyses suggest that the dominant magnetic carrier for the non-reddish sites (14XL19, 15XL23, and 15XL24) is magnetite with broad grain sizes and blocking temperatures. Over half of these grains are superparamagnetic at room temperature, inducing 'wasp-waisted' hysteresis loops, blurred to suppressed Verwey transition, and strong frequency-dependent magnetic susceptibility. Maghemitization is likely widespread in these grains. Fine-grained hematite is apparently common in these limestones. Small amounts of pyrrhotite and goethite are also apparent in some specimens. Pyrite, which alters on heating, is also
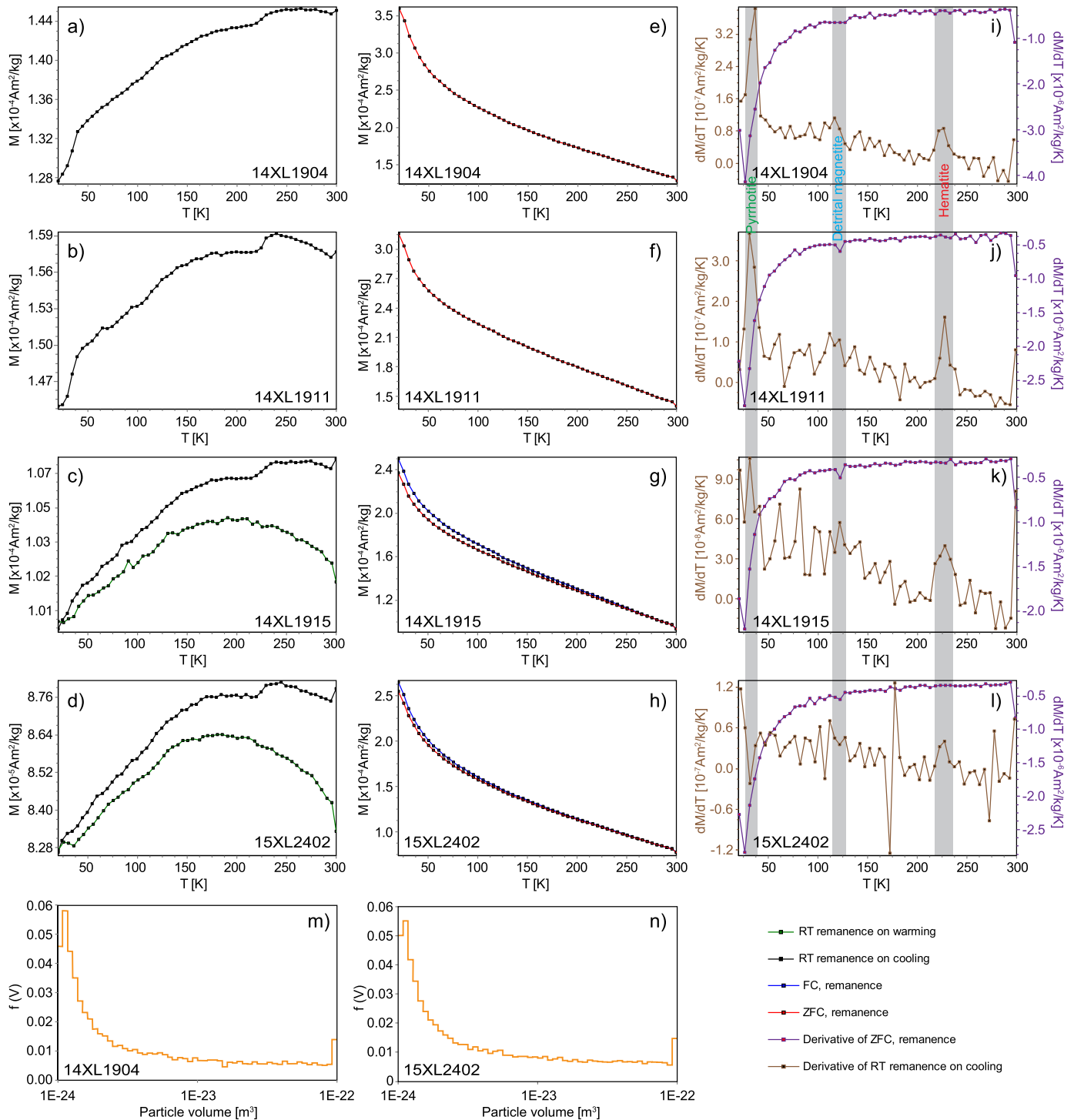
Fig. 7. (a–d) Low-temperature RTSIRM cycling curves at zero field for representative limestone specimens from sites 14XL19 and 15XL24. (e–h) Corresponding low-temperature SIRM warming curves in zero field after ZFC and FC treatments. (i–l) Corresponding derivatives of the RTSIRM cooling and ZFC SIRM warming curves. (m, n) Particle size distribution calculated from the ZFC SIRM curves in "e" and "h" (Worm and Jackson, 1999).

indicated by the behavior of some specimens. The reddish site 14XL20 most likely contains fined-grained hematite, with a suppressed Morin transition, as the dominant magnetic carrier and goethite as a minor magnetic phase.

5. SEM observation and EDS analysis

To visually and chemically characterize the magnetic minerals and their morphologies, which may provide an essential clue for

understanding their parageneses, we examined eight polished thin sections of specimens from these sites (three from 14XL19, one from 14XL20, three from 15XL23, and one from 15XL24) under the SEM at Peking University (Beijing, China) as used in a previous study (Huang et al., 2017a). EDS analysis was subsequently conducted after backscattered electron images were obtained.

For specimens from the non-reddish sites 14XL19, 15XL23, and 15XL24, the principal magnetic mineral identified under SEM is magnetite (Fig. 10; Fig. S1). The magnetite grains are subeuhedral
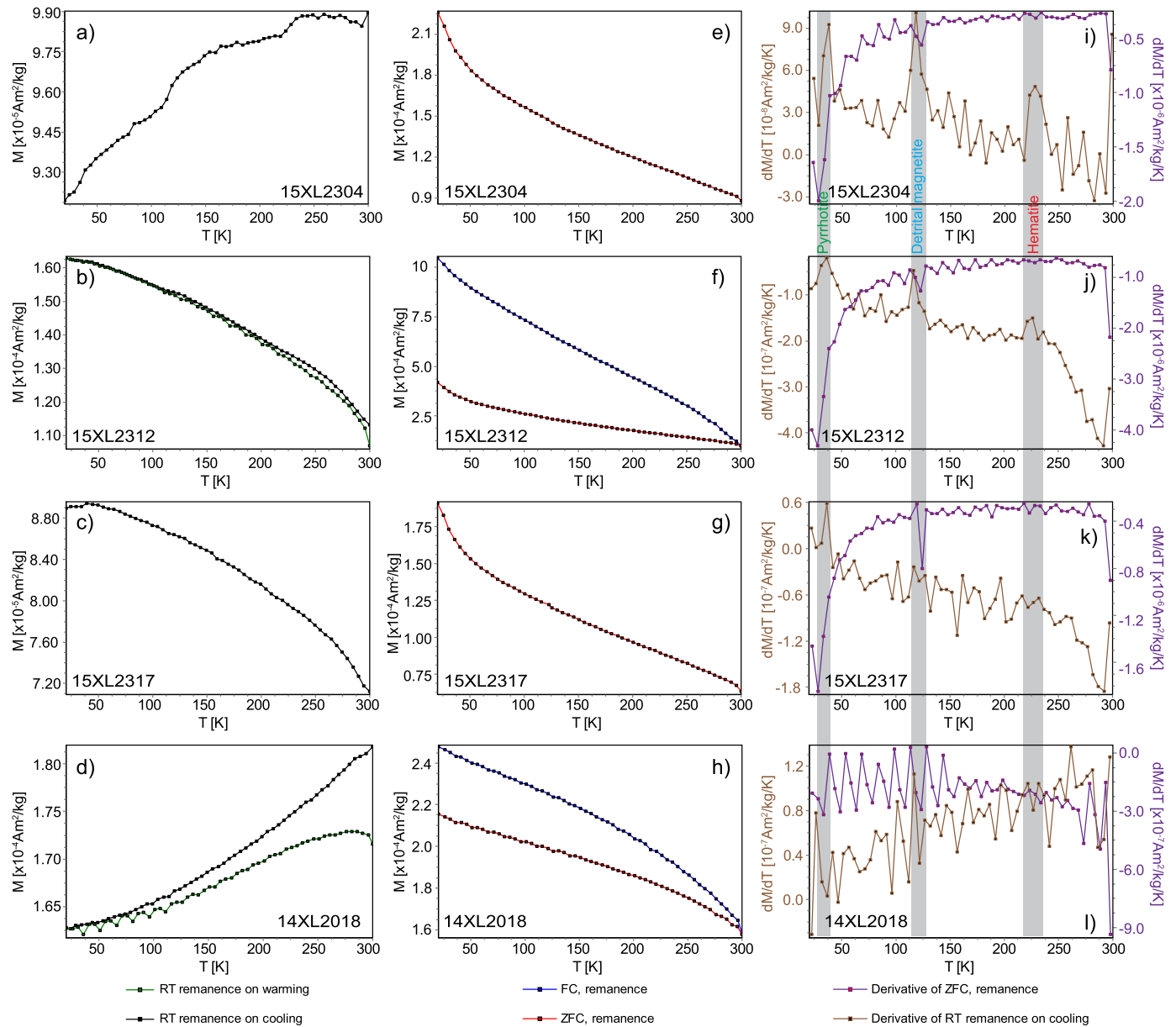
Fig. 8. (a–d) Low-temperature RTSIRM cycling curves at zero field for representative limestone specimens from sites 15XL23 and 14XL20. (e–h) Low-temperature SIRM warming curves in zero field after ZFC and FC treatments for specimens in "a"–"d". (i–l) Corresponding derivatives of the RTSIRM cooling and ZFC SIRM warming curves.

to euhedral or framboidal in shape with sizes less than 15 μm. Some magnetite shows growth zoning (Fig. 10k) and as rims surrounding pyrite grains (Fig. 10j). Pyrite is present as independent euhedral or framboidal grains (Figs. 10a, n), or is distributed typically in cores of fine-grained magnetite crystals in the framboids (Figs. 10b–f, i–l). These phenomena suggest that the magnetite grains are pseudomorphic after pyrite, and are probably an oxidation product of pyrite during later diagenetic events. Subrounded to rounded homogeneous magnetite is rarely found in the limestones. Minor rutile grains contain little iron (Fig. 10m), which may indicate that they formed after iron was leached from the lattice of detrital titanomagnetite during dissolution and diagenesis. The Fe/S ratios of some iron sulfide grains with diameter of ∼1 μm are between 0.5 and 1, suggesting a chemical composition of pyrrhotite or a mixture of pyrrhotite and pyrite (Figs. 10g, h). These Fe–S grains were possibly formed during desulphidation of pyrite (e.g., Rochette, 1987). Minor hematite or goethite cannot be discriminated from magnetite by SEM observations and EDS analyses in these specimens. For specimen from the reddish site 14XL20,

euhedral or framboidal aggregates composed of microcrystalline hematite and minor goethite are recognized by their characteristic platy morphology (Figs. 10o–t). The inner part of some aggregates are pseudomorphic after authigenic magnetite (Figs. 10p, t). These observations indicate that hematite or goethite are the additional oxidation products of pyrite.

6. Discussion

6.1. Evidence for the remagnetizations

Small variations in bedding orientation and the absence of a remanence at dual polarity of the sampled sites make it impossible to estimate the age and origin of the NRM by classic field tests. However, our comprehensive rock magnetic and petrographic results unequivocally indicate that these limestones were remagnetized due to growth of authigenic magnetic minerals and destruction of any pro-existing magnetic phases, which is a very prevailing mechanism for remagnetization (e.g., Elmore et al., 2012).
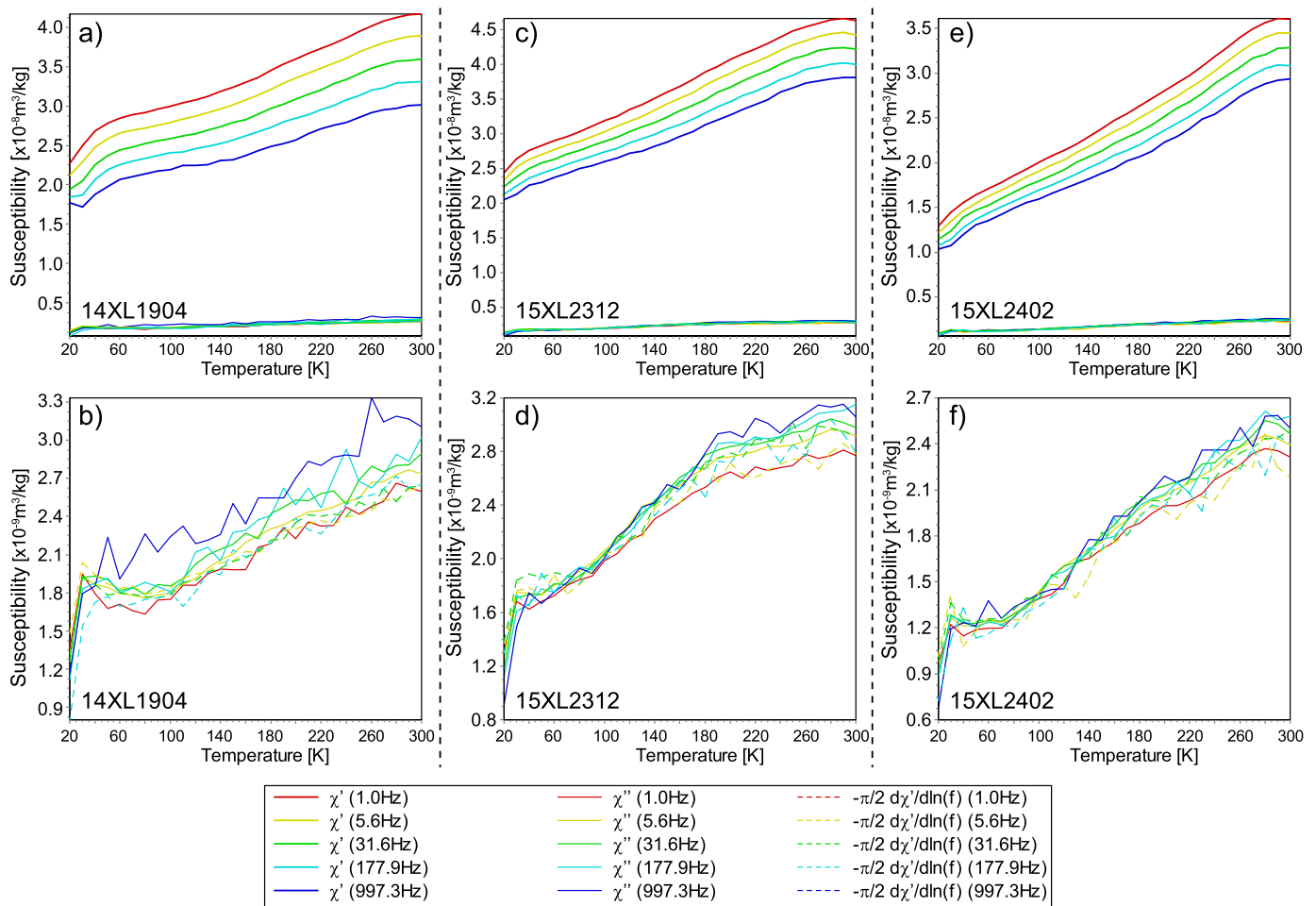
Fig. 9. (a, c, and e) Low-temperature in-phase and quadrature AC susceptibility measured from 20 to 300 K at different frequencies (1.0, 5.6, 31.6, 177.9, and 997.3 Hz) for 3 representative limestone specimens from three sites. (b, d, and f) Expanded view of quadrature susceptibilities, compared to the derivative of in-phase susceptibility with respect to $\ln(f)$.

The dominant magnetization carrier of the non-reddish sites 14XL19, 15XL23, and 15XL24 is magnetite with a broad range of unblocking temperature (Fig. 5). A large fraction of these magnetite grains is superparamagnetic as indicated by 'wasp-waisted' hysteresis loops at room temperature, by the loss of most of LTSIRM when warming up to room temperature, by a suppressed Verwey transition, and by strong frequency-dependence of magnetic susceptibility (Figs. 4–9). These features commonly fingerprint remagnetized carbonate rocks (Jackson and Swanson-Hysell, 2012, and references therein). Although the SP fraction does not contribute to NRM at room temperature, it is considered to have the same origin as the SSD or PSD particles which do carry the remanence in remagnetized carbonate rocks. Significant SP contribution and unimodal size distribution peaking at SP-SSD threshold below room temperature have been sometimes observed in carbonate rocks with extraterrestrial or extracellular magnetite (e.g., Lanci and Kent, 2006), but they are more often attributed to authigenesis in carbonate rocks (Jackson and Swanson-Hysell, 2012). Our SEM observations fully support that alteration of pre-existing pyrite and neoformation of magnetite are the reasons for remagnetization in the limestones we have examined (Fig. 10). More than half of the authigenic magnetite grains never grew larger than 25 nm in size, and are responsible for 'wasp-waisted' hysteresis loops and frequency-dependent susceptibility. The rest likely grew through the SP–SSD threshold at room temperature, inducing acquisition of a stable chemical remanent magnetization (CRM). The Verwey transition is suppressed for authigenic magnetite, which is possibly

related to its nonstoichiometric character due to maghemitization and its origin from pyrite oxidation (Jackson and Swanson-Hysell, 2012). The appearance of a weak Verwey transition in the RTSIRM cycling and LTSIRM warming curves of some specimens (Figs. 7, 8), especially these from site 15XL23, however, possibly indicates the existence of a small amount of detrital/biogenic magnetite, which may carry a primary NRM. The rutile grains we observe under SEM contain some iron, suggesting they might have formed by leaching of iron from detrital titanomagnetite during dissolution and alteration (Fig. 10). However, this potentially primary remanence overlaps with the unblocking temperatures and coercivities of the predominant authigenic magnetite, which probably makes it impossible to isolate it by thermal or alternating field demagnetization.

The reddish site 14XL20 is also remagnetized, as its main magnetic carriers are authigenic hematite and minor goethite pseudomorphic after pyrite. No detrital hematite was identified in these rocks. The remanent magnetization directions of this site are very different from these of other sites in both geographic and stratigraphic coordinates (Fig. 3), likely indicating another episode of remagnetization. Secondary magnetizations carried by hematite have been reported in a few studies (e.g., Elmore et al., 1993; Torsvik et al., 2005), and the rock magnetic character of these rocks and origin of hematite are not clear. Here we show that most hematite grains are nanoscaled with wide a unblocking temperature range (Figs. 5, 8). These hematite aggregates retain the morphology of pyrite, similar to authigenic magnetite pseudomorph
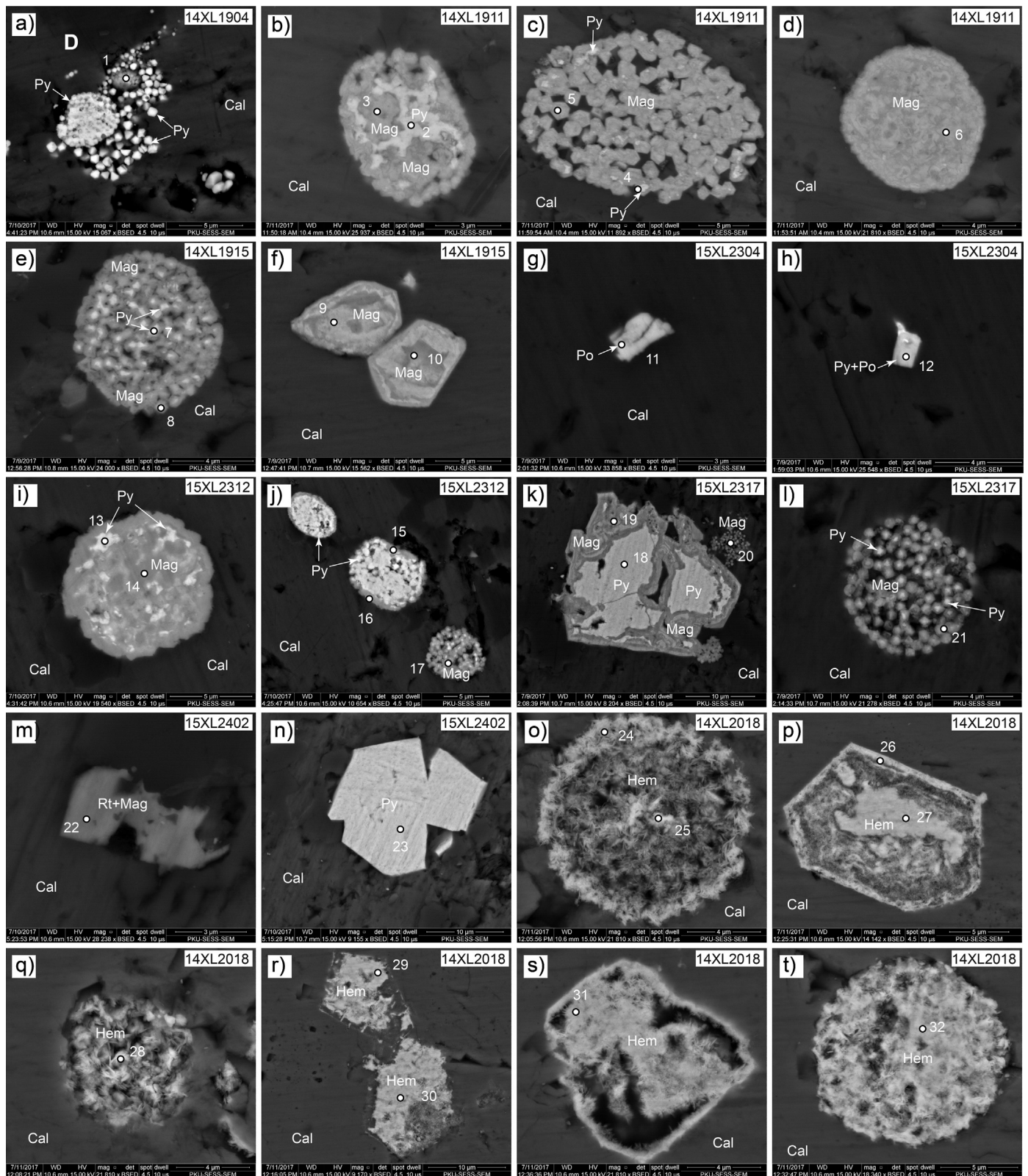
Fig. 10. SEM backscattered electron images of specimens from the Upper Triassic limestones. Mag: magnetite, Hem: hematite, Po: pyrrhotite, Cal: calcite, Py: pyrite, and Rt: rutile. White dots are the EDS analysis spots with the results shown in Fig. S1.

from pyrite, suggesting they result from further oxidation products of pyrite under higher oxygen fugacity. Two specimens from this site yield an ITC of reverse polarity (Fig. 3a). A robust reversals test cannot be applied because the number of independent results is too small, but it is quite clear that these two ITCs are nearly antipodal to the ITCs/HTCs of other specimens in this site. This suggests that the growth of authigenic hematite spanned a sufficiently long time in some specimens during both polarities. The

classic reversals test for these sites can therefore appear to be positive although both normal and reversed polarities are carried by remagnetizations.

The directions of the LTC isolated below 330 °C from these limestones differ from the ITC and HTC, but are indistinguishable from the PDF (Fig. 3a). This remanence is probably dominated by a recent thermoviscous component carried by authigenic magnetite or hematite. According to Néel's theory, this recent viscous overprint should be completely removed by 200 °C. The observed anomalously high unblocking temperatures may be attributed to the PSD/MD behavior of some authigenic magnetite and maghemitization (Jackson and Worm, 2001). Additionally, monoclinic pyrrhotite, recognized by our RTSIRM cycling curves (Figs. 7, 8) and SEM & EDS examinations (Fig. 10), may make a small contribution to the LTC. Production of authigenic monoclinic pyrrhotite is usually linked to diagenesis and metamorphism of pyrite-bearing sediments (Roberts, 2015), such as those found in metamorphosed belts of the Himalaya (Appel et al., 2012). This process is, however, extremely slow below 250 °C. The Triassic limestones in the Yushu-Nangqian area show no sign of metamorphism. Thus, it is likely that it occurred over the hundreds of millions of years since the deposition of these Triassic limestones.

6.2. Mechanism and timing of the remagnetizations

Based on our paleomagnetic, rock magnetic, and petrographic experiments, we distinguish three episodes of remagnetization in the Upper Triassic limestones in the Yushu-Nangqian area. The first one is expressed by oxidation of pyrite and neoformation of magnetite. We argue that it may be related to the collision between Qiangtang block and northeastern Tibet after the closure of Paleo-Tethys Oceans in the Late Triassic (Yin and Harrison, 2000; Song et al., 2015). Indeed, the ITCs isolated from the non-reddish sites 14XL19, 15XL23, and 15XL24 give a mean direction of $D_s/I_s = 36.4°/46.9°$. Comparing this direction to the robust Late Triassic paleopole of the Qiangtang block determined from volcanic rocks (204–213 Ma, Song et al., 2015) indicates a bedding dip of ∼7° at that time, suggesting that these limestones was only slightly tilted during the remagnetization. This is consistent with an early tectonic event initially bringing the limestones above sea level which would have dramatically changed the redox condition from reductive to oxidizing, inducing pyrite oxidation. As proposed for the Appalachian orogenic belt, this process may have been facilitated by orogenic fluids, either pumped by tectonic force or gravity; such fluids may have circulated through significant parts of the crust in the orogenic belt.

The secondary episode of remagnetization produced authigenic hematite and minor goethite in the reddish site. The distribution of these reddish limestones just below the unconformity between the Cenozoic red reds and Triassic strata strongly suggests that this episode of remagnetization was related to the development of a localized intra-mountain basin in northeastern Tibetan Plateau soon after India-Asia collision at ∼58 Ma (e.g., Hu et al., 2015). Considering a quasi-stable, coupled position of the Lhasa and Qiangtang blocks at ∼24°N at the sampling locality since early Cretaceous times (Lippert et al., 2014), the mean direction of this remanence of $D_g/I_g = 292°/53.6°$ implies that remagnetization occurred when bedding was tilted to ∼30°. Compared to the expected declination at the sampling locality from the Eurasian APWP (Torsvik et al., 2012), this further implies a counterclockwise rotation of ∼75° occurring after the remagnetization. The third episode is dominated by a recent thermoviscous overprint carried by authigenic magnetite or hematite initially formed in the first and secondary remagnetization episodes, and a minor CRM carried by authigenic monoclinic pyrrhotite with a protracted formation duration.

6.3. Implications for the preservation of primary NRM in the Tethyan carbonate rocks in the Tibetan Plateau

Preservation of primary NRM in sedimentary rocks depends on the long-term fate of magnetic minerals in the sediment during diagenesis. To discuss whether the Tethyan carbonate rocks in Tibet retain a primary NRM, we review those carbonate rocks that typically retain a primary NRM and provide high-fidelity records of the geomagnetic field (e.g., Channell and McCabe, 1994; Abrajevitch and Kodama, 2009; Chang et al., 2018). Those rocks are predominantly deep-water pelagic marine carbonates deposited far from the continents at water depths of 3000–6000 m and with depositional rates of <10 cm/kyr. Magnetic carriers in these rocks are dominated by biogenic SD magnetite and/or detrital PSD-MD magnetite and minor hematite (both aqueous and aeolian delivery). The early diagenesis in pelagic environments is more likely to be oxic because the organic matter is of low concentration (<0.2%) in these areas with low primary productivity and sedimentation rate and it can be consumed by the dissolved oxygen from the overlying bottom water (Roberts et al., 2013). Dissolved iron in pelagic bottom waters is limited (Boyd and Ellwood, 2010), so the formation of authigenic hematite or goethite is unlikely. Therefore, little diagenetic alteration affect the biogenetic or detrital magnetite or hematite, and the primary NRM is not likely to be contaminated by the CRM acquired by authigenic magnetic minerals. In the oxic conditions of later diagenesis or subaerial weathering, authigenic magnetic minerals, such as hematite or goethite, may still form at the expense of biogenetic or detrital magnetite in pelagic carbonates, leading to alteration of the primary NRM.

The Tethyan carbonates in the Tibetan Plateau were mostly deposited in shallow-water carbonate platform, ramp, and shelf settings with depths less than 350 m and depositional rate of ∼100 cm/kyr (Yin and Harrison, 2000). Organic carbon contents in these sediments could be as high as 10%, considering the high productivity at low latitudes where they were mostly located since the Carboniferous (Fig. 1b). Post-depositional degradation of the organic matter by microbial respiration consumes oxygen (oxic diagenesis), nitrate, manganese oxides, iron (oxyhydr)oxides, and sulphate in sequence until either all oxidants or all reactive organic matter is used up (Roberts et al., 2013). Therefore, in such environments, a sulphidic diagenetic environment would be created, during which detrital magnetite or hematite would be dissolved and iron sulphides, such as paramagnetic pyrite and minor ferrimagnetic greigite, would be formed by reaction of dissolved Fe^{2+} with dissolved HS^-. The primary NRM could thus be destroyed or overprinted during the early diagenesis. This process is ubiquitous in shallow-water carbonates with high organic carbon fluxes, and it explains why detrital (titano)magnetite and hematite are rarely preserved in the Triassic limestones we studied as well as Jurassic-Paleogene Tethyan Himalayan limestones (Huang et al., 2017a, 2017b), although the detrital input is higher in the shallow-water carbonates than that in the pelagic carbonates. In the later diagenetic stage, when the Tethyan carbonate rocks were tectonically uplifted above sea level due to orogenesis, following closure of Tethys Oceans, diagenesis changed from anoxic to suboxic and oxic, leading to oxidation of pyrite/greigite to magnetite/hematite/goethite and acquisition of CRM as identified in this study and the Tethyan Himalayan limestones (Huang et al., 2015, 2017a, 2017b). This process was probably assisted by continental-scale circulation of orogenic fluids through the shallow-water carbonates with high porosity (Jackson and Swanson-Hysell, 2012). Formation of authigenic monoclinic pyrrhotite during metamorphism is another important mechanism for the remagnetization of the metamorphic Tethyan carbonate rocks (Appel et al., 2012). Other mechanisms involving clay diagenesis in burial (e.g., Katz et al., 2000), organic maturation (Blumstein et al., 2004), and pressure solution (e.g., Elmore et al., 2006) may

also have occurred in the Tethyan carbonates. We speculate that these diagenetic processes are closely linked to the crustal shortening in the Tibetan Plateau and may have acted in concert with previous remagnetization processes, producing magnetic mineral alteration, and inducing pervasive remagnetization of Tethyan carbonates.

There are, however, examples of shallow-water carbonate rocks that retain a primary remanence. One is the Pleistocene Tahiti reef with significant detrital magnetite input from basalt of the nearby island (Ménabréaz et al., 2010). The other is Jurassic carbonate rocks in the Paris basin, which contain a significant amount of biogenic and detrital magnetite, as well as authigenic magnetite and goethite. There a refined paleomagnetic demagnetization procedure of AF ($<$10 mT), followed by thermal (up to 100–150 °C), and then AF demagnetization enabled the isolation of a primary remanence (Belkaaloul and Aïssaoui, 1997). In both examples, biogenic and/or detrital magnetite are found in exceptional abundance in these rocks. In most cases unfortunately, the contribution of the authigenic magnetite to the NRM cannot be distinguished from that of the primary biogenic and detrital (titano)magnetite, and a primary remanence cannot be sufficiently isolated. Considering the identified pervasive remagnetization in Tethyan carbonates in the Tibetan Plateau and contrasting depositional and diagenetic conditions of the Tethyan carbonate rocks compared to the pelagic carbonates, detailed rock magnetic and petrographic studies are strongly advised to identify the primary or secondary nature of the NRM, in addition to classic fold or reversals tests that may not facility to the detection of remagnetized rocks.

7. Conclusions

Paleomagnetic data for of carbonate rocks have played an important role in paleogeographic reconstructions of the Tibetan Plateau, yet these rocks often yield controversial results. We applied comprehensive rock magnetic measurements and SEM & EDS analyses to samples from upper Triassic carbonate rocks exposed in the Yushu-Nangqian area of the eastern Qiangtang block. Detrital magnetite, which may have carried the primary NRM, is rarely preserved in these rocks. On the contrary, we identified a main episode of regional remagnetization residing in authigenic magnetite (pseudomorphic after pyrite) from three non-reddish sites (14XL19, 15XL23, 15XL24), characterized by 'wasp-waisted' hysteresis loops, suppressed Verwey transitions, and strong frequency-dependent magnetic susceptibility. We propose that this remagnetization phase occurred early, in the Late Triassic, during the collision between the Qiangtang block and northeastern Tibetan Plateau. A second episode of remagnetization is recognized in one reddish site (14XL20) residing in authigenic hematite and minor goethite pseudomorphic after pyrite as well. This remagnetization is interpreted to relate to the localized Cenozoic basin development soon after India-Asia collision. The third remagentization is a combination of a recent thermoviscous overprint carried by authigenic magnetite and a CRM carried by authigenic pyrrhotite that may have formed very slowly since the Triassic. These episodes of remagnetization, if not recognized, would mistakenly yield either a lower paleolatitude (from the non-reddish sites 14XL19, 15XL23, and 15XL24) or higher paleolatitude (from the reddish site 14XL20) of the Qiangtang block after 100% bedding correction. Comparison between shallow-water Tethyan carbonate rocks in the Tibetan Plateau and primary remanence-carrying pelagic carbonate rocks indicates that they are very different in depositional and diagenetic conditions. Diagenesis has had limited effects on these pelagic carbonate rocks, whereas it had a controlling influence on the shallow-water carbonates on the continental margin. The possibility of preservation of primary NRM in the Tethyan

carbonates is thus not promising, but rock magnetic tests and petrographic examinations are necessary to diagnose insidious remagnetization.

Appendix A. Supplementary material

Supplementary material related to this article can be found online at https://doi.org/10.1016/j.epsl.2019.06.035.

References

Abrajevitch, A., Kodama, K., 2009. Biochemical vs. detrital mechanism of remanence acquisition in marine carbonates: a lesson from the K–T boundary interval. Earth Planet. Sci. Lett. 286, 269–277.

Appel, E., Crouzet, C., Schill, E., 2012. Pyrrhotite remagnetizations in the Himalaya: a review. Geol. Soc. (Lond.) Spec. Publ. 371, 163–180.

Belkaaloul, N.K., Aïssaoui, D.M., 1997. Nature and origin of magnetic minerals within the Middle Jurassic shallow-water carbonate rocks of the Paris Basin, France: implications for magnetostratigraphic dating. Geophys. J. Int. 130, 411–421.

Bian, W., Yang, T., Ma, Y., Jin, J., Gao, F., Zhang, S., Wu, H., Li, H., 2017. New Early Cretaceous palaeomagnetic and geochronological results from the far western Lhasa terrane: contributions to the Lhasa-Qiangtang collision. Sci. Rep. 7, 16216.

Blumstein, A.M., Elmore, R.D., Engel, M.H., Elliot, C., Basu, A., 2004. Paleomagnetic dating of burial diagenesis in Mississippian carbonates, Utah. J. Geophys. Res., Solid Earth 109, B04101. https://doi.org/10.1029/2003JB002698.

Boyd, P., Ellwood, M., 2010. The biogeochemical cycle of iron in the ocean. Nat. Geosci. 3, 675.

Cao, Y., Sun, Z., Li, H., Pei, J., Liu, D., Zhang, L., Ye, X., Zheng, Y., He, X., Ge, C., 2019. New paleomagnetic results from Middle Jurassic limestones of the Qiangtang terrane, Tibet: constraints on the evolution of the Bangong-Nujiang Ocean. Tectonics 38, 215–232. https://doi.org/10.1029/2017TC004842.

Chang, L., Harrison, R.J., Zeng, F., Berndt, T.A., Roberts, A.P., Heslop, D., Zhao, X., 2018. Coupled microbial bloom and oxygenation decline recorded by magnetofossils during the Palaeocene–Eocene Thermal Maximum. Nat. Commun. 9, 4007.

Channell, J., McCabe, C., 1994. Comparison of magnetic hysteresis parameters of unmagnetized and remagnetized limestones. J. Geophys. Res., Solid Earth 99, 4613–4623. https://doi.org/10.1029/93JB02578.

De Boer, C.B., Mullender, T.A., Dekkers, M.J., 2001. Low-temperature behaviour of haematite: susceptibility and magnetization increase on cycling through the Morin transition. Geophys. J. Int. 146, 201–216.

Dekkers, M., Mattéi, J.L., Fillion, G., Rochette, P., 1989. Grain-size dependence of the magnetic behavior of pyrrhotite during its low-temperature transition at 34 K. Geophys. Res. Lett. 16, 855–858. https://doi.org/10.1029/GL016i008p00855.

Dunlop, D.J., 2002. Theory and application of the Day plot (M_{rs}/M_s versus H_{cr}/H_c) 2. Application to data for rocks, sediments, and soils. J. Geophys. Res., Solid Earth 107, 2057. https://doi.org/10.1029/2001JB000487.

Dunlop, D.J., Özdemir, Ö., 1997. Rock Magnetism: Fundamentals and Frontiers. Cambridge University Press, Cambridge.

Elmore, R.D., London, D., Bagley, D., Fruit, D., Gao, G., 1993. Remagnetization by basinal fluids: testing the hypothesis in the Viola Limestone, southern Oklahoma. J. Geophys. Res., Solid Earth 98, 6237–6254. https://doi.org/10.1029/92JB02577.

Elmore, R.D., Foucher, J.L.-E., Evans, M., Lewchuk, M., Cox, E., 2006. Remagnetization of the Tonoloway Formation and the Helderberg Group in the Central Appalachians: testing the origin of syntilting magnetizations. Geophys. J. Int. 166, 1062–1076.

Elmore, R.D., Muxworthy, A.R., Aldana, M., 2012. Remagnetization and chemical alteration of sedimentary rocks. Geol. Soc. (Lond.) Spec. Publ. 371, 1–21.

Hu, X., Garzanti, E., Moore, T., Raffi, I., 2015. Direct stratigraphic dating of India–Asia collision onset at the Selandian (middle Paleocene, 59 ± 1 Ma). Geology 43, 859–862.

Huang, W., van Hinsbergen, D.J.J., Dekkers, M.J., Garzanti, E., Dupont-Nivet, G., Lippert, P.C., Li, X., Maffione, M., Langereis, C.G., Hu, X., Guo, Z., Kapp, P., 2015. Paleolatitudes of the Tibetan Himalaya from primary and secondary magnetizations of Jurassic to Lower Cretaceous sedimentary rocks. Geochem. Geophys. Geosyst. 16, 77–100. https://doi.org/10.1002/2014GC005624.

Huang, W., Lippert, P.C., Dekkers, M.J., Jackson, M.J., Zhang, Y., Li, J., Guo, Z., Kapp, P., van Hinsbergen, D.J.J., 2017a. Remagnetization of the Paleogene Tibetan Himalayan carbonate rocks in the Gamba area: implications for reconstructing the lower plate in the India–Asia collision. J. Geophys. Res., Solid Earth 122, 808–825. https://doi.org/10.1002/2016JB013662.

Huang, W., Lippert, P.C., Zhang, Y., Jackson, M.J., Dekkers, M.J., Li, J., Hu, X., Zhang, B., Guo, Z., Hinsbergen, D.J., 2017b. Remagnetization of carbonate rocks in southern Tibet: perspectives from rock magnetic and petrographic investigations. J. Geophys. Res., Solid Earth 122, 2434–2456. https://doi.org/10.1002/2017JB013987.

Jackson, M., Swanson-Hysell, N.L., 2012. Rock magnetism of remagnetized carbonate rocks: another look. Geol. Soc. (Lond.) Spec. Publ. 371, 229–251.

Jackson, M., Worm, H.-U., 2001. Anomalous unblocking temperatures, viscosity and frequency-dependent susceptibility in the chemically-remagnetized Trenton limestone. Phys. Earth Planet. Inter. 126, 27–42.

Kapp, P., DeCelles, P.G., Gehrels, G.E., Heizler, M., Ding, L., 2007. Geological records of the Lhasa-Qiangtang and Indo–Asian collisions in the Nima area of central Tibet. Geol. Soc. Am. Bull. 119, 917–933.

Katz, B., Elmore, R.D., Cogoini, M., Engel, M.H., Ferry, S., 2000. Associations between burial diagenesis of smectite, chemical remagnetization, and magnetite authigenesis in the Vocontian trough, SE France. J. Geophys. Res., Solid Earth 105, 851–868. https://doi.org/10.1029/1999JB900309.

Kirschvink, J., 1980. The least-squares line and plane and the analysis of palaeomagnetic data. Geophys. J. Int. 62, 699–718.

Kodama, K.P., 2012. Paleomagnetism of Sedimentary Rocks: Process and Interpretation. Wiley-Blackwell.

Koymans, M.R., Langereis, C.G., Pastor-Galán, D., van Hinsbergen, D.J., 2016. Paleomagnetism.org: an online multi-platform open source environment for paleomagnetic data analysis. Comput. Geosci. 93, 127–137.

Lanci, L., Kent, D.V., 2006. Meteoric smoke fallout revealed by superparamagnetism in Greenland ice. Geophys. Res. Lett. 33, L13308. https://doi.org/10.1029/2006GL026480.

Lippert, P.C., van Hinsbergen, D.J.J., Dupont-Nivet, G., 2014. The Early Cretaceous to Present latitude of the central Lhasa-plano (Tibet): a paleomagnetic synthesis with implications for Cenozoic tectonics, paleogeography and climate of Asia. In: Nie, J.S., Hoke, G.D., Horton, B.K. (Eds.), Towards an Improved Understanding of Uplift Mechanisms and the Elevation History of the Tibetan Plateau. In: Geological Society of America Special Paper, vol. 507. Geological Society of America, Boulder, Colorado, pp. 1–21.

Ma, Y., Yang, T., Bian, W., Jin, J., Wang, Q., Zhang, S., Wu, H., Li, H., Cao, L., 2018. A stable southern margin of Asia during the Cretaceous: paleomagnetic constraints on the Lhasa-Qiangtang collision and the maximum width of the Neo-Tethys. Tectonics 37, 3853–3876. https://doi.org/10.1029/2018TC005143.

Ma, Y., Wang, Q., Wang, J., Yang, T., Tan, X., Dan, W., Zhang, X., Ma, L., Wang, Z., Hu, W., 2019. Paleomagnetic constraints on the origin and drift history of the North Qiangtang Terrane in the Late Paleozoic. Geophys. Res. Lett. 46, 689–697. https://doi.org/10.1029/2018GL080964.

Ménabréaz, L., Thouveny, N., Camoin, G., Lund, S.P., 2010. Paleomagnetic record of the late Pleistocene reef sequence of Tahiti (French Polynesia): a contribution to the chronology of the deposits. Earth Planet. Sci. Lett. 294, 58–68.

Özdemir, Ö., Dunlop, D.J., 2010. Hallmarks of maghemitization in low-temperature remanence cycling of partially oxidized magnetite nanoparticles. J. Geophys. Res., Solid Earth 115, B02101. https://doi.org/10.1029/2009JB006756.

Özdemir, Ö., Dunlop, D.J., Berquo, T.S., 2008. Morin transition in hematite: size dependence and thermal hysteresis. Geochem. Geophys. Geosyst. 9, Q10Z01. https://doi.org/10.1029/2008GC002110.

Roberts, A.P., 2015. Magnetic mineral diagenesis. Earth-Sci. Rev. 151, 1–47.

Roberts, A.P., Florindo, F., Chang, L., Heslop, D., Jovane, L., Larrasoaña, J.C., 2013. Magnetic properties of pelagic marine carbonates. Earth-Sci. Rev. 127, 111–139.

Rochette, P., 1987. Metamorphic control of the magnetic mineralogy of black shales in the Swiss Alps: toward the use of "magnetic isogrades". Earth Planet. Sci. Lett. 84, 446–456.

Song, P., Ding, L., Li, Z., Lippert, P.C., Yang, T., Zhao, X., Fu, J., Yue, Y., 2015. Late Triassic paleolatitude of the Qiangtang block: implications for the closure of the Paleo-Tethys Ocean. Earth Planet. Sci. Lett. 424, 69–83.

Song, P., Ding, L., Li, Z., Lippert, P.C., Yue, Y., 2017. An early bird from Gondwana: paleomagnetism of Lower Permian lavas from northern Qiangtang (Tibet) and the geography of the Paleo-Tethys. Earth Planet. Sci. Lett. 475, 119–133.

Spurlin, M.S., Yin, A., Horton, B.K., Zhou, J., Wang, J., 2005. Structural evolution of the Yushu-Nangqian region and its relationship to syncollisional igneous activity, east-central Tibet. Geol. Soc. Am. Bull. 117, 1293–1317. https://doi.org/10.1130/B25572.1.

Tauxe, L., Mullender, T., Pick, T., 1996. Potbellies, wasp-waists, and superparamagnetism in magnetic hysteresis. J. Geophys. Res., Solid Earth 101, 571–583. https://doi.org/10.1029/95JB03041.

Torsvik, T., Pandit, M., Redfield, T., Ashwal, L., Webb, S., 2005. Remagnetization of Mesozoic limestones from the Jaisalmer basin, NW India. Geophys. J. Int. 161, 57–64.

Torsvik, T.H., Van der Voo, R., Preeden, U., Mac Niocaill, C., Steinberger, B., Doubrovine, P.V., van Hinsbergen, D.J.J., Domeier, M., Gaina, C., Tohver, E., 2012. Phanerozoic polar wander, palaeogeography and dynamics. Earth-Sci. Rev. 114, 325–368.

van der Voo, R., Torsvik, T.H., 2012. The history of remagnetization of sedimentary rocks: deceptions, developments and discoveries. Geol. Soc. (Lond.) Spec. Publ. 371, 23–53.

van Hinsbergen, D.J.J., Lippert, P.C., Dupont-Nivet, G., McQuarrie, N., Doubrovine, P.V., Spakman, W., Torsvik, T.H., 2012. Greater India Basin hypothesis and a two-stage Cenozoic collision between India and Asia. Proc. Natl. Acad. Sci. USA 109, 7659–7664.

Worm, H.U., 1998. On the superparamagnetic-stable single domain transition for magnetite, and frequency dependence of susceptibility. Geophys. J. Int. 133, 201–206.

Worm, H.U., Jackson, M., 1999. The superparamagnetism of Yucca Mountain Tuff. J. Geophys. Res., Solid Earth 104, 25415–25425. https://doi.org/10.1029/1999JB900285.

Yin, A., Harrison, M.T., 2000. Geologic evolution of the Himalayan–Tibetan orogen. Annu. Rev. Earth Planet. Sci. 28, 211–280.

Zegers, T., Dekkers, M., Bailly, S., 2003. Late Carboniferous to Permian remagnetization of Devonian limestones in the Ardennes: role of temperature, fluids, and deformation. J. Geophys. Res., Solid Earth 108, 2357. https://doi.org/10.1029/2002JB002213.

Zhou, Y., Cheng, X., Yang, X., Peng, X., Xue, Y., Ye, Y., Li, Y., Dong, H., Wu, H., 2017. A constraint on the Tethyan evolution: new evidence from Triassic paleomagnetic results in the Qiangtang Terrane, Tibetan Plateau, China. China Sciencepaper, pp. 1–13.